

Chapter - 3
Synthesis and
Photoluminescence Studies
of Strontium Cerium
Niobate Nanophosphor

3.1 Introduction

Pervoskite generally outlines a kind of the crystal structure with chemical formula ABX_3 , in which A and B are cations while X is an anion. In an ideal cubic structure, A cation has 12-fold cuboctahedral coordination. B cation has 6-fold coordination surrounded by an octahedron of anions. The cubic unit cell of such compounds is composed of A cations at cube-corner positions, B occupying at the body-center location, and X anion obtaining the face-centered positions [1]. Oxide pervoskites are in use in various ferroelectric [2, 3], piezoelectric [4 – 6], dielectric [7 – 9], pyroelectric applications [10, 11], and LED [12, 13] etc.

At present high efficient luminescent phosphors are synthesized by various methods like hydrothermal, sol-gel, combustion, solid state reaction, etc. For increasing the effectiveness of white light emission in solid-state devices, maximum attention has been given to develop new phosphors in the near-UV range [14, 15]. Sr_2CeNbO_6 shows very efficient luminescence properties in the UV–blue region of the spectrum due to the energy level difference between the $4f^1$ and $5d^1$ configurations of Ce^{3+} [16, 17].

Hydrothermal synthesis of ceramic powders has interesting potential in view of increasing demand for environmentally benign materials and manufacturing methods. Hydrothermal reactions are usually performed in moderate conditions, which do not require expensive precursors or equipment and may yield homogeneous crystalline powders [14, 18]. Now, hydrothermal technology has found its place in several branches of science and technology, covering a variety of fields, such as materials science, earth science, metallurgy, physics, chemistry, biology, etc. Given the broad application and increasing importance of the hydrothermal method, it has been improved considerably during a process of continuous development [19]. For example, the application of microwaves [20, 21], mechanical mixing [22, 23], and electric fields [24, 25] to enhance the reaction kinetics of the hydrothermal method had appeared in widespread attention. With these techniques, the experimental time has been reduced by at least two orders of magnitude, making this technology more economical and practical. Hydrothermal synthesis involves water as a catalyst and occasionally as a component of solid phases in the synthesis at elevated temperature ($>100^\circ C$) and pressure (greater than a few atmospheres). It is nontoxic, nonflammable, noncarcinogenic, nonmutagenic, and thermodynamically stable. Another advantage of hydrothermal is that water is very volatile, so it can be removed from the product very easily [14].

Hydrothermal method to synthesis pervoskite-type oxides have attracted a vast deal of interest for numerous years now; however, the report shows the existence of a large difference in ionic radii of B-cations of double pervoskite-type oxides [26 – 30].

The common materials used for synthesis of Strontium Cerium Niobate (SCN) are Strontium Carbonate (SrCO_3), Cerium (III) Nitrate Hexahydrate ($\text{Ce}(\text{NO}_3)_3 \cdot 6\text{H}_2\text{O}$) and Niobium Oxide (Nb_2O_5). Cerium Nitrate Hexahydrate is a highly water soluble crystalline Cerium source for uses compatible with nitrates and lower (acidic) pH [31]. Nitrate compounds are generally soluble in water and these materials are also oxidizing agents. Nitrates are excellent precursors for production of ultra-high purity compounds and certain catalyst and nanoscale (nanoparticles and nanopowders) materials.

The interest to study the Nb_2O_5 is due to its remarkable physicochemical properties and structural isotropy suitable for a wide range of applications in the construction of gas sensing, and photoelectrodes, as well as in field-emission displays and microelectronics [32]. Niobium Oxide Nanocrystals include in electrochemical capacitors and electrochemical cathodes, nanowire, nanofibre and catalyst applications. Niobium oxide also uses as niobium oxide nanotubes, their potential electrical, magnetic, optical, and biomedical and bioscience properties [33].

The pervoskite structure is adopted by many oxides that have the chemical formula ABO_3 . The most common pervoskite compounds contain oxygen and there are a few pervoskite compounds that form without oxygen. Niobium based pervoskite oxides have been found very useful for various industrial and technological applications [34]. The study of electrical properties of these materials provides useful information regarding their stability in electrical and electronic devices.

Practically all kinds of optical centres have been studied in the pervoskite structure for low as well as in high concentration. The optical studies on pervoskite systems have contributed considerably to the development of many optical materials like LASER materials, solar energy conversion, and many more [35].

3.2 Synthesis and Characterization

3.2.1 Synthesis

Strontium Cerium Niobate (SCN) was synthesized by the hydrothermal method. The starting materials are AR grade Strontium carbonate (SrCO_3 , purity 99%), Cerium Nitrate Hexahydrate ($\text{Ce}(\text{NO}_3)_3 \cdot 6\text{H}_2\text{O}$, purity 99%) and Niobium Pentoxide (Nb_2O_5 , purity 99.95 %) taken in a stoichiometric ratio of 0.2M SrCO_3 , 0.2M Nb_2O_5 , and 0.2M

$\text{Ce}(\text{NO}_3)_3 \cdot 6\text{H}_2\text{O}$. Each is dissolved in 100 ml distilled water. As a solution of $\text{Ce}(\text{NO}_3)_3 \cdot 6\text{H}_2\text{O}$ was kept under continuous stirring, the solution of Nb_2O_5 and SrCO_3 was added drop wise in it. The resultant solution was prepared by stirring using a magnetic stirrer at room temperature. Taking 75ml solution mixture after 10-minute stirring with the remaining solution under continuous stirring, then continued to draw different samples after 20 min., 40 min., and 80 min of a time interval. The amount of each sample taken is about 75 ml. All the samples were dried at 70°C for 2 hours in an oven. Figure.1 shows the flow chart of the hydrothermal method used to synthesize $\text{Sr}_2\text{CeNbO}_6$ (SCN).

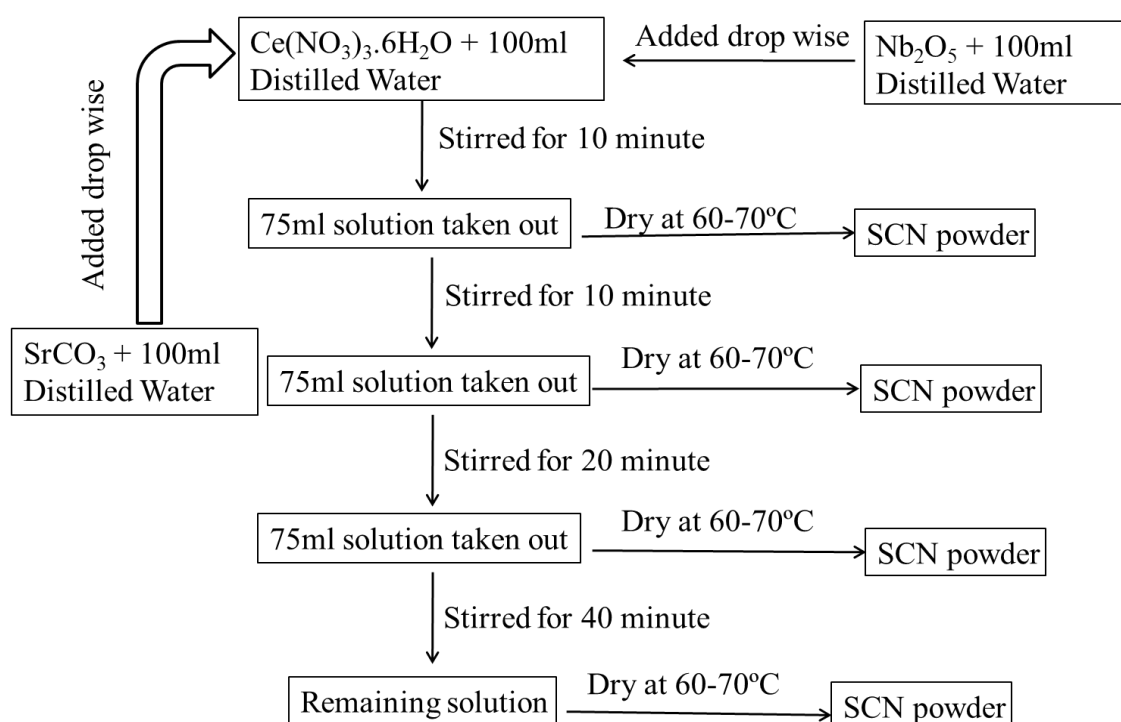


Figure 3.1 Flow chart of $\text{Sr}_2\text{CeNbO}_6$ synthesis method.

3.2.2 Characterization

XRD measurements were done on D8 Bruker advance X-Ray Diffractometer with the $\text{Cu K}\alpha$ radiation having wavelength of 1.5443 \AA and energy 8.05 keV . The intensity versus angle (2θ) graph gives the information about the variation of intensity and having the peaks at some 2θ angles. FTIR spectra recorded on a Jasco FTIR- 4100, spectrophotometer (Japan) by mixing with KBr in mortar and pestle in the ratio of 1:10. PL emission spectra done at room temperature the light from a xenon lamp through a monochromator was used for the optical excitation. Here PL spectra recorded by Shimadzu spectrophotofluorometer.

3.3 Results And Discussion

3.3.1 X-Ray Diffraction

Double-pervoskites with lanthanide ordered on one subset of the octahedrally coordinated B sites have recently been of crystal-chemical interest. The magnetic lanthanide sub lattice presents a classical *fcc* arrangement, and the edge-shared network of lanthanide octahedra is known to result in geometric magnetic defeat. As X-ray diffraction (XRD) is a non-destructive technique for phase identification, XRD patterns are especially important for phase characterization [36].

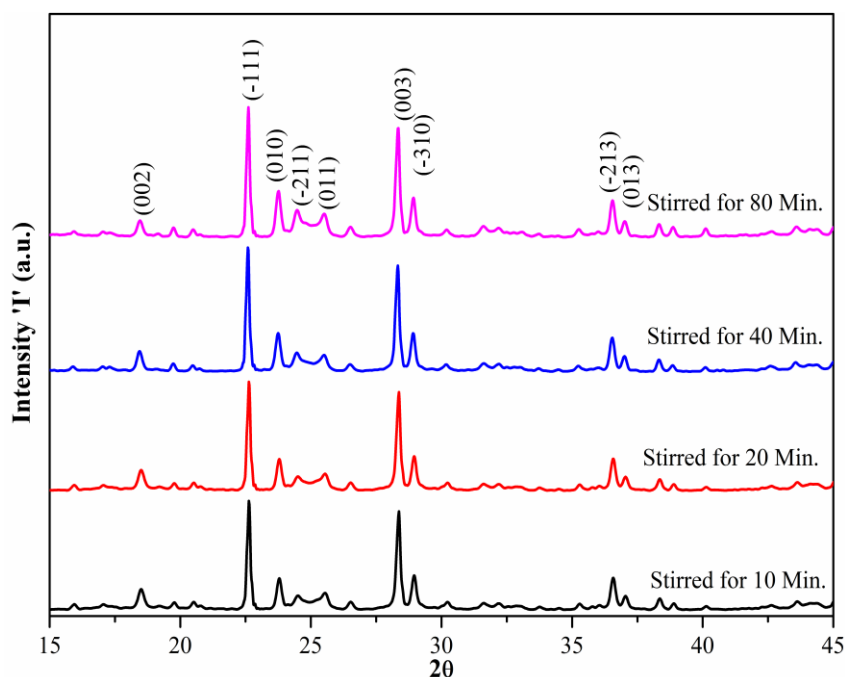


Figure 3.2 X-Ray Diffraction patterns of $\text{Sr}_2\text{CeNbO}_6$ phosphors.

Figure 3.2 presents the X-ray diffraction (XRD) pattern of $\text{Sr}_2\text{CeNbO}_6$. As stirring time increased, the intensity and crystallinity of $\text{Sr}_2\text{CeNbO}_6$ also increased. The phosphors that have high crystallinity always means few defects and also have stronger luminescence [37]. All the reflection peaks of the X-ray profile are indexed, and lattice parameters are determined with the help of a standard computer program Powder – X. Inter-planer spacing (d-spacing) suggests that all phosphors have a monoclinic structure with space group $P2_1/n$ at room temperature [38, 39]. The relative coordinates and occupancy of each site for $\text{Sr}_2\text{GdNbO}_6$ are shown in Table 3.1. The values for the bond distances of cations (relative to the oxygen anion) and occupancy were obtained from the Rietveld refinement [40]. These are shown in Table 3.2. These diffraction lines are consistent and confirm the formation of a double pervoskite structure for all studied samples. XRD pattern confirms a single pervoskite phase for all phosphors. Table 3.3

shows the Summary of cell parameter, volume and crystalline size of Sr₂CeNbO₆ samples. Average crystalline size of all sample are calculated by using Scherrer formula which was given below [41].

$$D = \frac{k*\lambda}{\beta*Cos\theta} \dots\dots\dots (3.1)$$

Where, λ = wavelength of X-ray i.e. 1.5443Å, θ = Diffraction angle, k = constant 0.94 and β = FWHM

Atom	Site	X	Y	Z
Sr	4e	0.5258	0.5732	0.2465
Ce	2c	0.0000	0.5000	0.0000
Nb	2d	0.5000	0.0000	0.0000
O	4e	0.2228	0.1742	-0.0552
O	4e	0.3333	0.7255	-0.0553
O	4e	0.3895	-0.0199	0.2231

Table 3.1 Structural parameters of Sr₂CeNbO₆ found by Rietveld analysis of XRD data.

Cation	Anion & Multi.	Distance (Å)	Occupancy
Ce (2c)	O (4e) X 2	2.4052	1.00
Ce (2c)	O (4e) X 2	2.4098	1.00
Ce (2c)	O (4e) X 2	2.4074	1.00
Nb (2d)	O (4e) X 2	1.9766	1.00
Nb (2d)	O (4e) X 2	1.9802	1.00
Nb (2d)	O (4e) X 2	1.9765	1.00
Sr (4e)	O (4e) X 1	3.9149	1.00
Sr (4e)	O (4e) X 1	3.0182	1.00
Sr (4e)	O (4e) X 1	2.6499	1.00
Sr (4e)	O (4e) X 1	2.5127	1.00
Sr (4e)	O (4e) X 1	2.9124	1.00
Sr (4e)	O (4e) X 1	3.9290	1.00
Sr (4e)	O (4e) X 1	2.5509	1.00
Sr (4e)	O (4e) X 1	2.7238	1.00
Sr (4e)	O (4e) X 1	3.4415	1.00
Sr (4e)	O (4e) X 1	2.4823	1.00
Sr (4e)	O (4e) X 1	3.6900	1.00
Sr (4e)	O (4e) X 1	2.5989	1.00

Table 3.2 Inter-atomic distance and occupancy calculated through Rietveld refinement of experimental data.

Williamson-Hall Plot

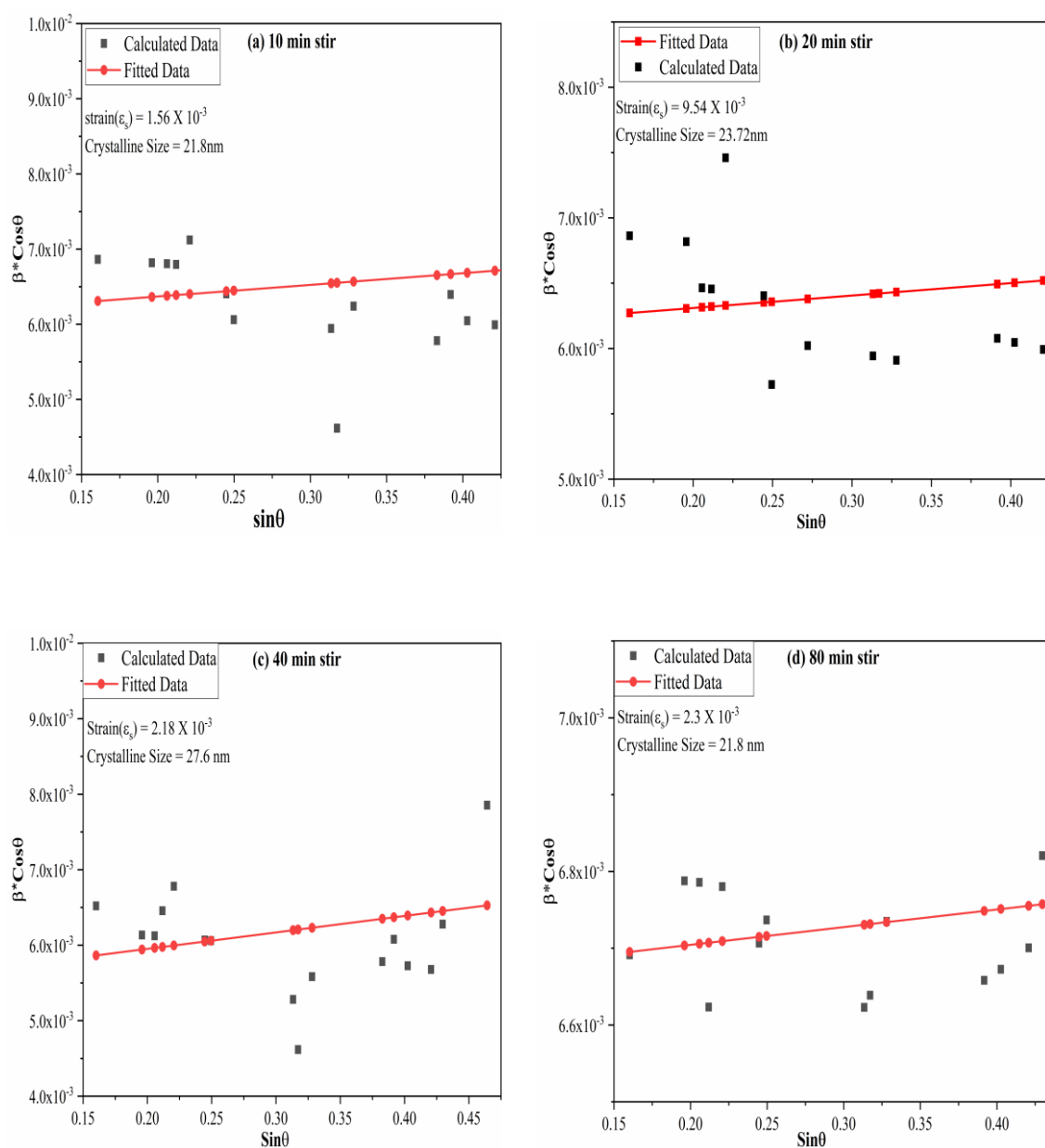


Figure 3.3 Williamson – Hall Plot of $\text{Sr}_2\text{CeNbO}_6$ phosphors.

From various kinds of crystal defects, the one we are concerned about here is a non-uniform strain because it is the characteristic of the cold-worked state of metals and alloys. The change in the shape of any grain is determined not only by the applied forces to the section as a whole but also by the fact that each grain retains contact on its side surfaces with all its neighbours [42]. Because of this cooperation between grains, a single grain in a polycrystalline section is not free to deform in the same way as an isolated single crystal. As a result of this restraint by its neighbours, a plastically

deformed grain in a solid, usually has regions of its lattice left in an elastically bent or twisted condition or rarely, in a state of uniform tension or compression [43].

The phosphor is then said to contain residual stress. Such stress is usually called internal stress but the term is not very informative since all stress residual or externally imposed are internal. The term residual stress indicates the fact that the stress remains after all external forces are removed [44]. These kinds of stress are also known as micro stress since they differ from one grain to another or from one part of the grain to another part on a microscopic scale. On the other hand, the stress may be quite uniform over large distances; it is then referred to as macro stress [45].

The broadening effect of XRD peaks reflects the nano crystalline nature of the resulting $\text{Sr}_2\text{CeNbO}_6$ samples. Since the effective XRD peak broadening can be caused by lattice strain and small crystallite size, these two effects have to be distinguished. This can be calculated by plotting $\beta \cos\theta$ versus $\varepsilon \sin\theta$ in the following relation (Williamson–Hall plot) [41].

$$\beta_{hkl} * \cos\theta_{hkl} = \left(\frac{k*\lambda}{D}\right) + \varepsilon * \sin\theta_{hkl} \dots\dots\dots (3.2)$$

The shift in the XRD patterns is also reflected in the Williamson–Hall plot, which is attributed due to the highly strained and distorted environment in the $\text{Sr}_2\text{CeNbO}_6$ lattice. Strain and crystalline size obtain from W-H plot listed in Table 3.3.

Sample		$\text{Sr}_2\text{CeNbO}_6$ 10 min Stir	$\text{Sr}_2\text{CeNbO}_6$ 20 min Stir	$\text{Sr}_2\text{CeNbO}_6$ 40 min Stir	$\text{Sr}_2\text{CeNbO}_6$ 80 min Stir
Structure		Monoclinic	Monoclinic	Monoclinic	Monoclinic
Space Group		P2 ₁ /n	P2 ₁ /n	P2 ₁ /n	P2 ₁ /n
Cell	a(Å)	5.6258	5.7258	5.7186	5.7246
Parameters	b(Å)	5.4865	5.4326	5.4432	5.4326
	c(Å)	9.3256	9.3256	9.3318	9.3215
	B	91.256	90.856	90.833	90.752
Volume (Å)³		287.77	290.05	290.48	289.89
Average	Scherrer	22.1	23.87	27.42	21.59
Crystalline	Method				
Size (nm)	W-H Plot	21.8	23.72	27.6	21.8
Strain (ε)		1.56 X 10 ⁻³	9.54 X 10 ⁻³	2.18 X 10 ⁻³	2.3 X 10 ⁻³

Table 3.3 Summary of cell parameter, volume and crystallite size of $\text{Sr}_2\text{CeNbO}_6$.

3.3.2 FTIR (Fourier Transform Infrared Spectrometry)

In infrared spectroscopy, as IR radiation is transferred through a sample, some IR radiation is absorbed while some of it transmitted by the sample. The resulting spectra depict the absorption and transmission line of a molecule, produced a molecular fingerprint of the sample. Like a fingerprint, two unique molecular structures never give the same infrared spectrum. This makes infrared spectroscopy useful for different types of analysis [46].

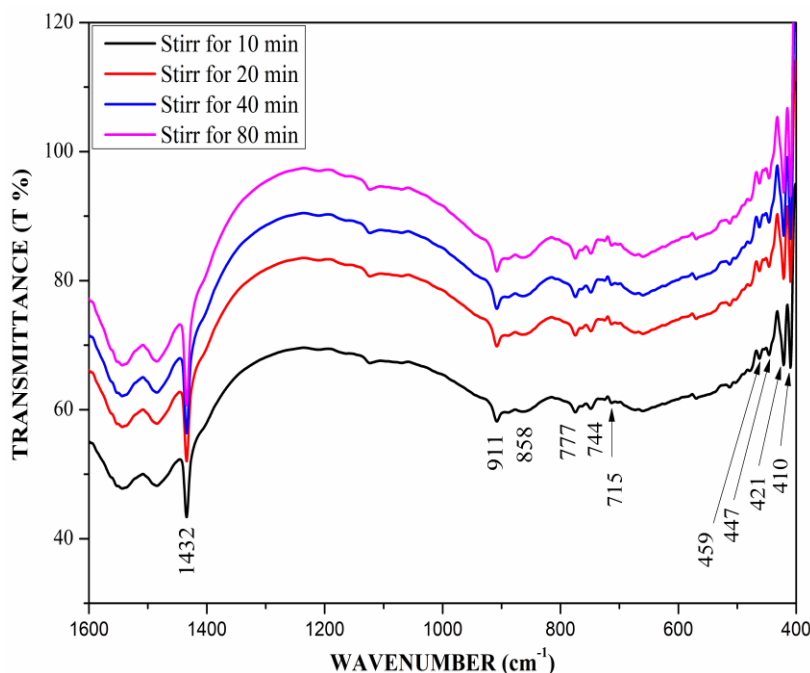


Figure 3.4 FTIR spectra of $\text{Sr}_2\text{CeNbO}_6$ phosphors.

Figure 3.4 shows FTIR spectra of $\text{Sr}_2\text{CeNbO}_6$ with a range of wavenumber from 400 cm^{-1} to 1600 cm^{-1} . The IR spectrum of $\text{Sr}_2\text{CeNbO}_6$ shows some well-defined bands in Figure 3.4. This is in good accordance with what is systematically found for a perovskite structure following group theory prophecies [47]. In this type of material, significant vibrational couplings between the different coordination polyhedral structures may be expected. The observed shoulder peak at 715 cm^{-1} recommends the overlapping of Sr_2O_6 and NbO_6 stretching bands with the displacement toward higher frequencies of the NbO_6 bands [48].

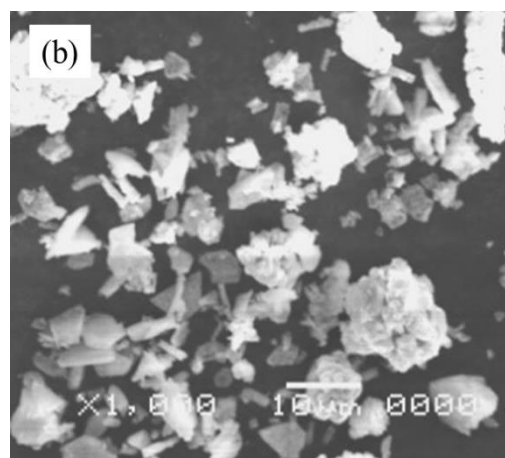
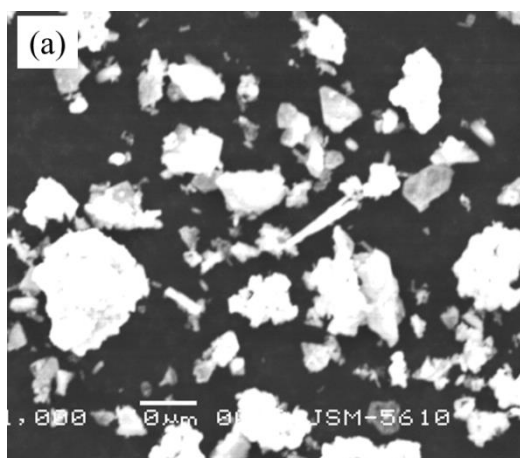
Several perovskite-type oxides and especially the niobium containing compounds may present corner-shared and edge-shared octahedra [49, 50]. Corner-shared and edge-shared octahedra are predominant in niobium-oxygen polyhedral compounds, where edge-shared octahedra exhibit large distortions than corner-shared

Octahedra which appearing in significant alterations in Nb-O bond lengths, for the edge-shared octahedral [51 – 53]. The Nb-O bond length varies from 1.7 to 2.3 Å, whereas in corner-shared octahedra Nb-O bond lengths are in the range of 1.9 to 2.1 Å [54, 55].

In the case of the end edge-shared NbO₆ octahedra, the symmetric stretching vibrations are usually observed in the range of 850-1000 cm⁻¹, whereas in the corner shared octahedra these vibrations are observed in 750-850 cm⁻¹ region [56, 57]. The same spectral pattern, with two strong and well-defined IR bands in the 400-750 cm⁻¹ region, had been found in a large number of A₂BB'O₆ perovskite type materials, and they were assigned in the same way [58, 59]. In the present study, the symmetric stretching vibrations from 911 cm⁻¹, completely support the possible presence of edge-connected Nb-O octahedra.

3.3.3 SEM (Scanning Electron Microscopy)

Figure 3.5 (a) - (d) shows SEM images of SCN for stirring time of 10, 20, 40, and 80 minutes. SEM images exhibited that the particle size and morphology diversified with the alternating stirring time of Sr₂CeNbO₆ at the same reaction temperature. Figure 3.5 (a) shows particles of SCN producing numerous types of shapes like hexagonal, needle, flowered, etc. This different variety of shapes is uniquely obtained. As the stirring time increases, the shape of SCN particles becomes unique, but the size of the particle also differs as shown in Figure 3.5 (b). As stirring time increases at room temperature, cotton flower type shape occurred, which presented in Figure 3.5 (c) and (d).



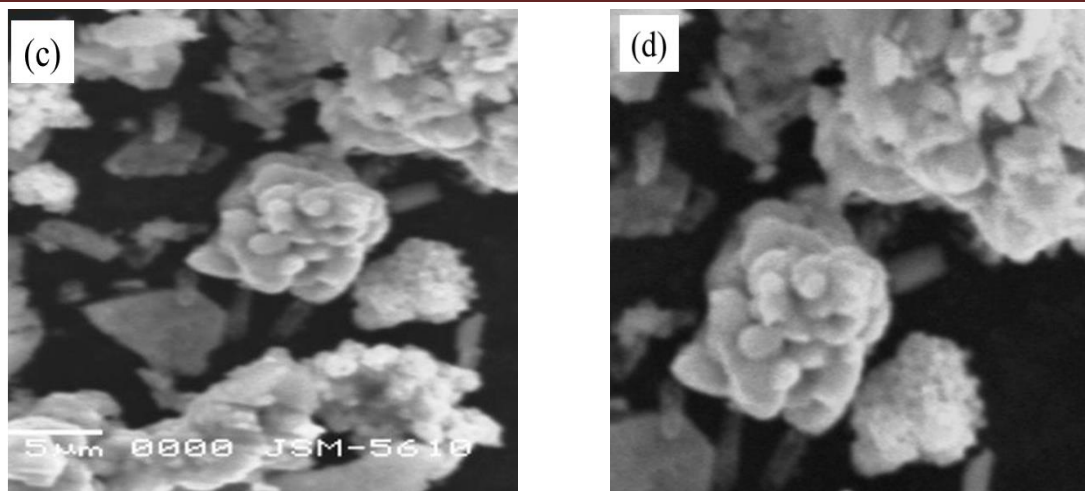


Figure 3.5 (a), (b), (c), and (d) SEM image of $\text{Sr}_2\text{CeNbO}_6$ phosphors for 10 min., 20 min., 40 min., and 80 min. stirring time respectively.

3.3.4 Photoluminescence

The luminescence properties of the samples have been examined by recording the Photoluminescence spectra. To study the grain size, the effect of $4f \rightarrow 5d$ inter-configurational transitions, room temperature emission, and excitation spectra are recorded [60]. The PLE spectrum shows strong, and broad-ranging band from 230 to 380 nm and towering at 316 nm, which is attributed to $\text{Ce}^{3+} 4f \rightarrow 5d$ transition and matched well with the emission of Near UV chips [61].

To obtain excellent photoluminescence intensity at room temperature, most of these oxides have to be activated with a trivalent lanthanide ion or a combination of ions [62]. Photoluminescence is strongly reliant on the concentration of doping, where Photoluminescence was activated by doping and concentration quenching typically seen when doping levels exceeds 5 to 10% [62 – 64]. Also, charge neutrality plays an important function in improving the luminescence efficiency of phosphors.

Figure 3.6 shows the PLE and PL spectra were recorded at room temperature of Strontium Ceria Niobate (SCN). A broad emission band occurred corresponding to the parity-allowed electric dipole transition ($5d \rightarrow 4f$). The emission spectra were compounded by broad and asymmetric band emission centered at about 394 nm attributed to the transition, from the lowest of the crystal field component of $5d^1$ to the two levels of the ground state $^2F_{5/2}$ and $^2F_{7/2}$ [60].

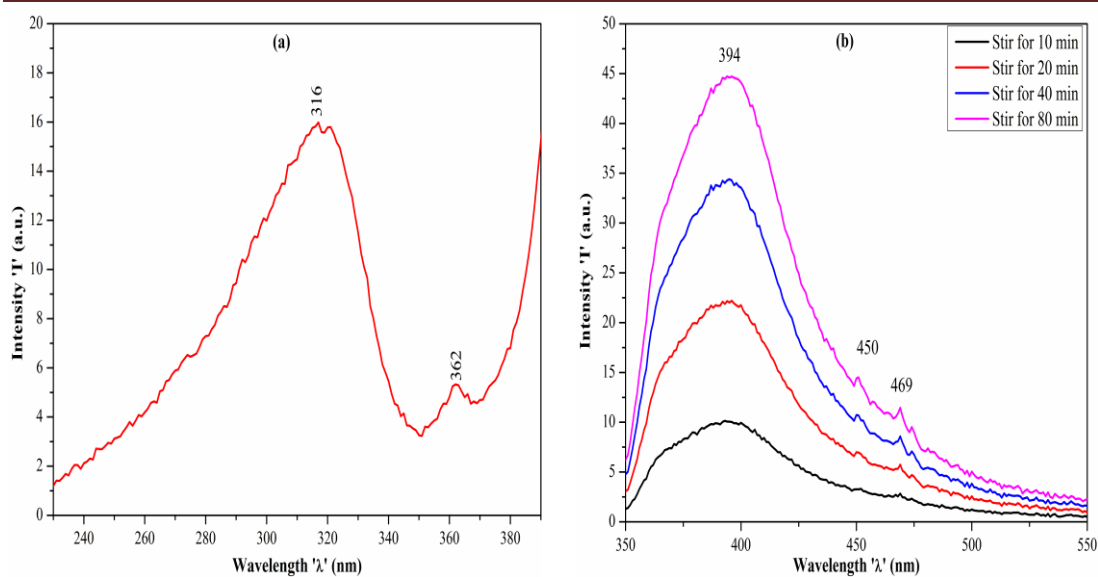


Figure 3.6 (a) Excitation spectra of Sr₂CeNbO₆ and (b) Emission spectra of Sr₂CeNbO₆.

The PLE spectra measured for 400 nm emission wavelength are shown in Figure 3.6. The excitation spectra exhibit two absorption bands: the first one is very intense and centered at 316nm, and the second is a low-intensity band centered at 362 nm. These bands can be attributed to the allowed electric-dipole transitions from $4f^1$ ground state to the 5d excited states of the Ce⁺³ ion [65, 66]. It is well understood that the electron in 5d state experiences more effective interactions with the crystal field related to the electron in 4f state because of the large radial extension of the 5d orbitals [67]. Furthermore, the 4f - 5d excitation and emission bands are widely vibronic; consequently the decomposition of emission and excitation spectra into a sum of Gaussian curves is justified [68].

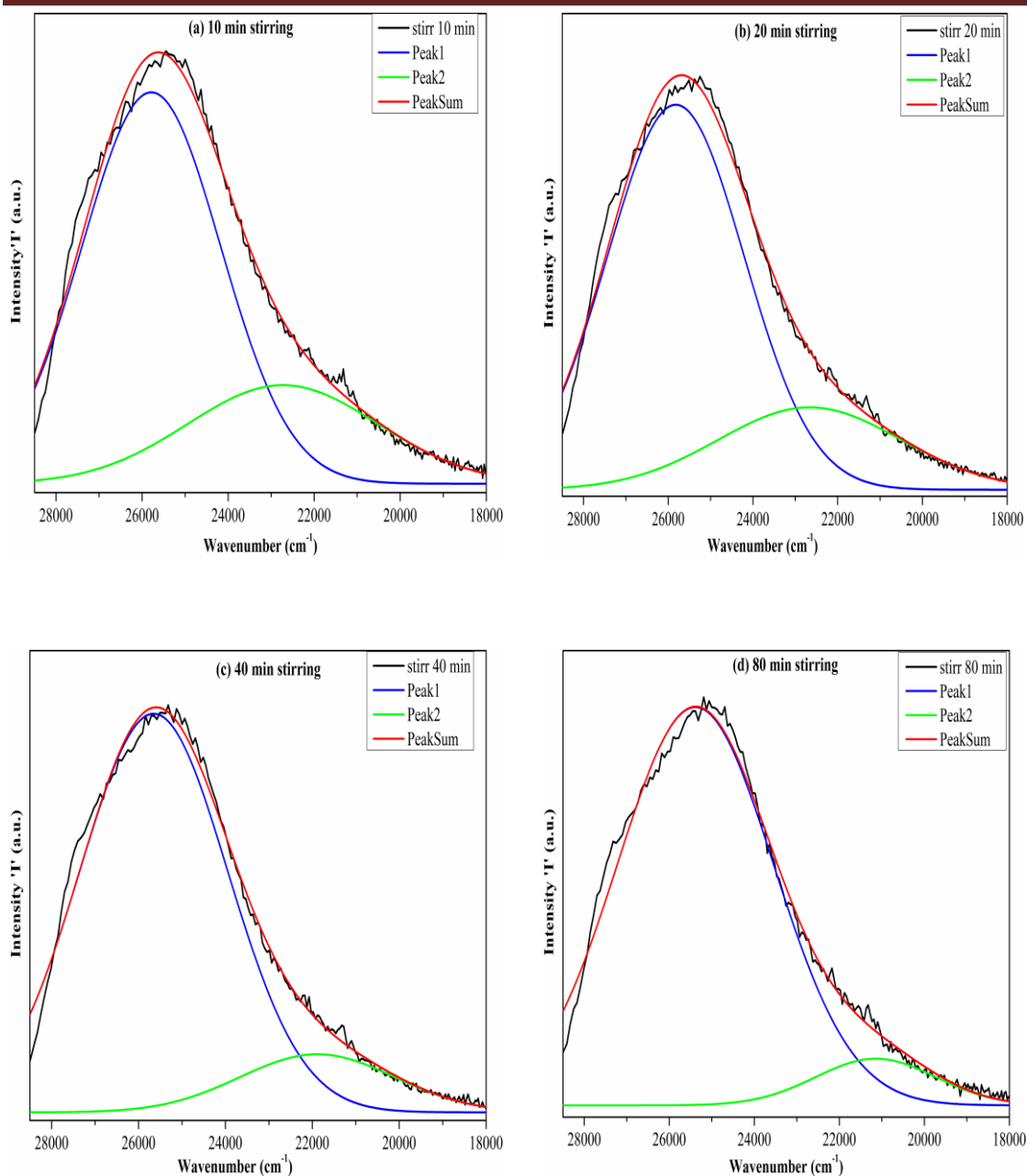


Figure 3.7 Decomposition into sum of two Gaussian curves of different stirring time emission spectra of $\text{Sr}_2\text{CeNbO}_6$.

Figure.3.7 shows the emission spectra of SCN nanophosphor, fitted into two Gaussian curves represent the $5d \rightarrow 2F_{5/2}, 2F_{7/2}$ inter-configurational transitions at room temperature. From Figure.3.7 we noted that the high energy transition ($5d \rightarrow 2F_{5/2}$) shows the same intensity compared to the lower energy ($5d \rightarrow 2F_{7/2}$) [69].

The emission spectra show two shoulder peaks at 450nm and at 469nm with energies 2.75eV and 2.645eV respectively. As the stirring time increased the shoulder

peaks generated prominently the optical transitions that occurred in Ce^{+3} from $5d$ to $4f$, which are relatively fast ($\sim 20\text{--}40$ ns) [70, 71].

CIE (Commission Internationale de l'Éclairage)

Commission Internationale de l'Éclairage (CIE) chromaticity coordinate for all Sr_2CeNbO_6 phosphors had been calculated using the xenon lamp with the excitation wavelength 254 nm shown in Figure 3.8 and the coordinate values are found in the blue region. Their coordinate point had been indicated in Figure 3.8 with a cross in the blue region. This clearly shows that Sr_2CeNbO_6 sample can be used for blue colored solid-state lighting applications, and its chromaticity coordinate is listed in Table 3.4 [72].

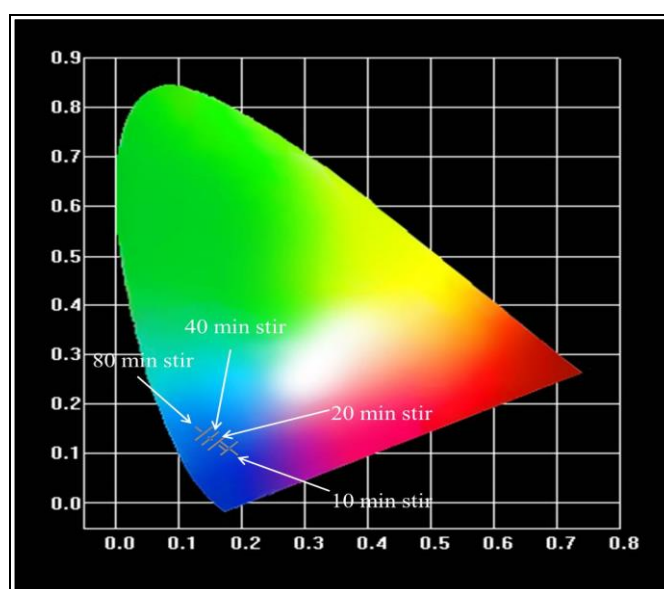


Figure 3.8 CIE 1931 for all Sr_2CeNbO_6 phosphors.

Sample	CIE coordinate		CCT	
	X	y	Calculated	Software
Sr_2CeNbO_6 for 10 min stir	0.18	0.11	2621.4	2715
Sr_2CeNbO_6 for 20 min stir	0.16	0.12	4171.1	4182
Sr_2CeNbO_6 for 40 min stir	0.15	0.13	5870.9	5912
Sr_2CeNbO_6 for 80 min stir	0.14	0.14	6962.7	6980

Table 3.4 CIE coordinate and CCT of Sr_2CeNbO_6 at 254nm emission spectra.

3.4. Outcome

Double Pervoskite phosphor Strontium Cerium Niobate (SCN) oxide present in this chapter has been synthesizing by the hydrothermal method. The X-ray diffraction measurement of Strontium Cerium Niobate (SCN) oxide reveals that phosphor has a monoclinic phase with space group P21/n (# 014). Prepared pervoskite phosphor is nanocrystalline measured through Scherrer's method and Williamson-hall plot method. Shifting in XRD patterns is also reflected in the Williamson–Hall plot, which occurred due to the highly strained and distorted environment in the $\text{Sr}_2\text{CeNbO}_6$ lattice. FTIR of $\text{Sr}_2\text{CeNbO}_6$ gives information that phosphor has a nano-size pervoskite structure with an edge-connected Nb-O octahedral. The observed shoulder peak at 715 cm^{-1} recommends the overlapping of Sr_2O_6 and NbO_6 stretching bands with the displacement toward higher frequencies of the NbO_6 bands. The symmetric stretching vibrations from 911 cm^{-1} completely support the possible presence of edge-connected Nb-O octahedra. SEM image shows that $\text{Sr}_2\text{CeNbO}_6$ phosphors have different shapes and sizes with initial stir time. With increasing stir time, phosphor had been appearing as cotton flower-shaped type particles. Room temperature photoluminescence spectra of phosphor recorded using a Xenon lamp as a source. The emission spectra appeared as broad and asymmetric band emission centered at about 394 nm attributed to the transition. The intensity of this broad peak increases with an increase in stir time. The emission spectra of SCN nanophosphor fitted into two Gaussian curves, which represent the $^5\text{d} \rightarrow ^2\text{F}_{5/2}, ^2\text{F}_{7/2}$ inter-configurational transitions at room temperature. The CIE coordinates values situated in the blue region. It recognized that the $\text{Sr}_2\text{CeNbO}_6$ samples are applicable for blue-colored solid-state lighting applications.

References

- [1] A. K. Jena, A. Kulkarni, and T. Miyasaka, "Halide Pervoskite Photovoltaics: Background, Status, and Future Prospects," *Chem. Rev.*, vol. 119, no. 5, pp. 3036–3103, Mar. 2019.
- [2] H. Röhm, T. Leonhard, A. D. Schulz, S. Wagner, M. J. Hoffmann, and A. Colmann, "Ferroelectric Properties of Pervoskite Thin Films and Their Implications for Solar Energy Conversion," *Adv. Mater.*, vol. 31, no. 26, p. 1806661, Jun. 2019.
- [3] N. Nuraje and K. Su, "Pervoskite ferroelectric nanomaterials," *Nanoscale*, vol. 5,

- no. 19, p. 8752, 2013.
- [4] H. Wang *et al.*, “Large piezoelectric response in a family of metal-free perovskite ferroelectric compounds from first-principles calculations,” *npj Comput. Mater.*, vol. 5, no. 1, p. 17, Dec. 2019.
- [5] Y.-M. You *et al.*, “An organic-inorganic perovskite ferroelectric with large piezoelectric response,” *Science (80-.)*, vol. 357, no. 6348, pp. 306–309, Jul. 2017.
- [6] J. Hao, W. Li, J. Zhai, and H. Chen, “Progress in high-strain perovskite piezoelectric ceramics,” *Mater. Sci. Eng. R Reports*, vol. 135, pp. 1–57, Jan. 2019.
- [7] W. Ming, H. Shi, and M.-H. Du, “Large dielectric constant, high acceptor density, and deep electron traps in perovskite solar cell material CsGeI₃,” *J. Mater. Chem. A*, vol. 4, no. 36, pp. 13852–13858, 2016.
- [8] J. N. Wilson, J. M. Frost, S. K. Wallace, and A. Walsh, “Dielectric and ferroic properties of metal halide perovskites,” *APL Mater.*, vol. 7, no. 1, p. 010901, Jan. 2019.
- [9] A. K. Yadav and C. Gautam, “Dielectric behavior of perovskite glass ceramics,” *J. Mater. Sci. Mater. Electron.*, vol. 25, no. 12, pp. 5165–5187, Dec. 2014.
- [10] Y. Bai, T. Siponkoski, J. Peräntie, H. Jantunen, and J. Juuti, “Ferroelectric, pyroelectric, and piezoelectric properties of a photovoltaic perovskite oxide,” *Appl. Phys. Lett.*, vol. 110, no. 6, p. 063903, Feb. 2017.
- [11] R. Moalla *et al.*, “Large anisotropy of ferroelectric and pyroelectric properties in heteroepitaxial oxide layers,” *Sci. Rep.*, vol. 8, no. 1, p. 4332, Dec. 2018.
- [12] T. Matsushima *et al.*, “High performance from extraordinarily thick organic light-emitting diodes,” *Nature*, vol. 572, no. 7770, pp. 502–506, Aug. 2019.
- [13] Y. Liu *et al.*, “Efficient blue light-emitting diodes based on quantum-confined bromide perovskite nanostructures,” *Nat. Photonics*, vol. 13, no. 11, pp. 760–764, Nov. 2019.
- [14] D. Tawde, M. Srinivas, and K. V. R. Murthy, “Effect of lead source and cerium (III) doping on structural and photoluminescence properties of PbWO₄ microcrystallites synthesized by hydrothermal method,” *Phys. status solidi*, vol. 208, no. 4, pp. 803–807, Apr. 2011.
- [15] Z. C. Wu, J. X. Ā. Shi, J. Wang, M. L. Ā. Gong, and Q. Su, “A novel blue-emitting phosphor LiSrPO₄: Eu²⁺ for white LEDs,” vol. 179, pp. 2356–2360,

- 2006.
- [16] D. Hou, B. Han, W. Chen, H. Liang, and Q. Su, "Luminescence of Ce³⁺ at two different sites in α -Sr₂P₂O₇ under vacuum ultraviolet-UV and x-ray excitation ultraviolet-UV and x-ray excitation," vol. 083527, no. May, 2012.
- [17] G. Blasse and B. C. Grabmaier, *Luminescent Materials*. Berlin, Heidelberg: Springer Berlin Heidelberg, 1994.
- [18] D. Modi, M. Srinivas, D. Tawde, K. V. R. Murthy, V. Verma, and N. Patel, "Hydrothermal synthesis and photoluminescence properties of cerium-doped cadmium tungstate nanophosphor," *J. Exp. Nanosci.*, vol. 0, no. 0, pp. 1–11, Apr. 2014.
- [19] G. Yang and S.-J. Park, "Conventional and Microwave Hydrothermal Synthesis and Application of Functional Materials: A Review," *Materials (Basel)*, vol. 12, no. 7, p. 1177, Apr. 2019.
- [20] R. S. Melo, F. C. Silva, K. R. M. Moura, A. S. de Menezes, and F. S. M. Sinfrônio, "Magnetic ferrites synthesised using the microwave-hydrothermal method," *J. Magn. Magn. Mater.*, vol. 381, pp. 109–115, May 2015.
- [21] Z. Li *et al.*, "Synthesizing SnTe nanocrystals leading to thermoelectric performance enhancement via an ultra-fast microwave hydrothermal method," *Nano Energy*, vol. 28, pp. 78–86, Oct. 2016.
- [22] W. Yuan *et al.*, "In situ hydrothermal synthesis of a novel hierarchically porous TS-1/modified-diatomite composite for methylene blue (MB) removal by the synergistic effect of adsorption and photocatalysis," *J. Colloid Interface Sci.*, vol. 462, pp. 191–199, Jan. 2016.
- [23] D. D. Athayde *et al.*, "Review of perovskite ceramic synthesis and membrane preparation methods," *Ceram. Int.*, vol. 42, no. 6, pp. 6555–6571, May 2016.
- [24] M. Sheikholeslami, S. Soleimani, and D. D. Ganji, "Effect of electric field on hydrothermal behavior of nanofluid in a complex geometry," *J. Mol. Liq.*, vol. 213, pp. 153–161, Jan. 2016.
- [25] M. Sheikholeslami and R. Ellahi, "Electrohydrodynamic Nanofluid Hydrothermal Treatment in an Enclosure with Sinusoidal Upper Wall," *Appl. Sci.*, vol. 5, no. 3, pp. 294–306, Aug. 2015.
- [26] D. Modi, M. S. D. Tawde, S. Garg, D. Khatri, and K. V. R. Murthy, "Photoluminescence Investigation of CdWO₄: Ce, Er doped nano Phosphors," vol. 2, no. I, pp. 9–11, 2012.

- [27] A. Dias and V. S. T. Ciminelli, "Electroceraic Materials of Tailored Phase and Morphology by Hydrothermal Technology," *Chem. Mater.*, vol. 15, no. 6, pp. 1344–1352, Mar. 2003.
- [28] J. Spooren, A. Ruplecker, F. Millange, and R. I. Walton, "Subcritical Hydrothermal Synthesis of Pervoskite Manganites: A Direct and Rapid Route to Complex Transition-Metal Oxides," *Chem. Mater.*, vol. 15, no. 7, pp. 1401–1403, Apr. 2003.
- [29] L. Wu, X. Mei, and W. Zheng, "Hydrothermal synthesis and characterization of double pervoskite Ba₂YSbO₆," *Mater. Lett.*, vol. 60, no. 19, pp. 2326–2330, Aug. 2006.
- [30] T. Zhang, C. G. Jin, T. Qian, X. L. Lu, J. M. Bai, and X. G. Li, "Hydrothermal synthesis of single-crystalline La_{0.5}Ca_{0.5}MnO₃ nanowires at low temperature," *J. Mater. Chem.*, vol. 14, no. 18, p. 2787, 2004.
- [31] J. Dahle and Y. Arai, "Environmental Geochemistry of Cerium: Applications and Toxicology of Cerium Oxide Nanoparticles," *Int. J. Environ. Res. Public Health*, vol. 12, no. 2, pp. 1253–1278, Jan. 2015.
- [32] A. M. Raba, J. Bautista-Ruíz, and M. R. Joya, "Synthesis and Structural Properties of Niobium Pentoxide Powders: A Comparative Study of the Growth Process," *Mater. Res.*, vol. 19, no. 6, pp. 1381–1387, Oct. 2016.
- [33] M. J. OLSZTA, J. WANG, and E. C. DICKEY, "Stoichiometry and valence measurements of niobium oxides using electron energy-loss spectroscopy," *J. Microsc.*, vol. 224, no. 3, pp. 233–241, Dec. 2006.
- [34] M. A. Peña and J. L. G. Fierro, "Chemical Structures and Performance of Pervoskite Oxides," *Chem. Rev.*, vol. 101, no. 7, pp. 1981–2018, Jul. 2001.
- [35] R. K. Sajwan, S. Tiwari, T. Harshit, and A. K. Singh, "Recent progress in multicolor tuning of rare earth-doped gadolinium aluminate phosphors GdAlO₃," *Opt. Quantum Electron.*, vol. 49, no. 11, p. 344, Nov. 2017.
- [36] W. Wong-Ng, J. A. Kaduk, M. Luong, and Q. Huang, "X-ray diffraction study and powder patterns of double-pervoskites Sr₂RSbO₆ (R = Pr, Nd, Sm, Eu, Gd, Dy, Ho, Y, Er, Tm, Yb, and Lu)," *Powder Diffr.*, vol. 29, no. 4, pp. 371–378, Dec. 2014.
- [37] N. Kunkel, A. D. Sontakke, S. Kohaut, B. Viana, and P. Dorenbos, "Thermally Stimulated Luminescence and First-Principle Study of Defect Configurations in the Pervoskite-Type Hydrides LiMH₃:Eu²⁺ (M = Sr, Ba) and the

- Corresponding Deuterides,” *J. Phys. Chem. C*, vol. 120, no. 51, pp. 29414–29422, Dec. 2016.
- [38] B. Ghosh, A. Dutta, and T. P. Sinha, “Vibrational modes and electrical transport in Sr₂GdTaO₆,” *Mater. Chem. Phys.*, vol. 143, no. 1, pp. 26–33, Dec. 2013.
- [39] A. Dutta and T. P. Sinha, “Dielectric Relaxation and Electronic Structure of Double Perovskite Ca₂AlNbO₆,” *Integr. Ferroelectr.*, vol. 116, no. July 2015, pp. 41–50, 2010.
- [40] M. W. Lufaso and P. M. Woodward, “Prediction of the crystal structures of perovskites using the software program SPuDS,” *Acta Crystallogr. Sect. B*, vol. 57, no. 6, pp. 725–738, 2001.
- [41] C. Suryanarayana and M. G. Norton, *X-Ray Diffraction*, 1st ed. Boston, MA: Springer US, 1998.
- [42] R. Jacob and I. Jayakumari, “X-ray diffraction line profile analysis of Ba Sr_{0.6} Fe_{0.4} TiO₃ (BSFTO),” *Int. J. Chem. Stud.*, vol. 5, no. 2, pp. 12–21, 2015.
- [43] S. Eatih, “A Study of the Effect of Processing Variables on the Mechanical Properties of 5 inch Cartridge Cases,” NAVAL POSTGRADUATE SCHOOL, 1982.
- [44] Y. Du, C. Lü, M. Destrade, and W. Chen, “Influence of Initial Residual Stress on Growth and Pattern Creation for a Layered Aorta,” *Sci. Rep.*, vol. 9, no. 1, p. 8232, Dec. 2019.
- [45] B. D. Cullity, *Elements of X-Ray Diffraction*, 1st ed. MASSACHUSETTS: ADDISON-WESLEY PUBLISHING COMPANY, Inc., 1956.
- [46] T. Nicolet and C. All, “Introduction to Fourier Transform Infrared Spectrometry,” 2001.
- [47] M. Licheron, F. Gervais, J. Coutures, and J. Choisnet, “‘Ba₂BiO₄’ surprisingly found as a cubic double perovskite,” *Solid State Commun.*, vol. 75, no. 9, pp. 759–763, Sep. 1990.
- [48] A. E. Lavat and E. J. Baran, “IR-spectroscopic characterization of A₂BB₀O₆ perovskites,” vol. 32, pp. 167–174, 2003.
- [49] C. N. R. Rao and J. Gopalakrishnan, *New Directions in Solid State Chemistry*. Cambridge University Press, 1997.
- [50] M. L. Craus, I. Rusu, and A. Rusu, “ON SOME MIXED OXIDES IN THE SYSTEM CaO-CdO-Bi₂O₃-Nb₂O₅. CATION DISTRIBUTION IN A DISTORTED AURIVILLIUS STRUCTURE – I calc obs calc,” vol. 5, no. 3, pp.

- 653–656, 2003.
- [51] S. Jaulmes, S. Launay, P. Mahé, and M. Quarton, “Silicatoniobate de Potassium, $K_3Nb_3O_6Si_2O_7$,” *Acta Crystallogr. Sect. C Cryst. Struct. Commun.*, vol. 51, no. 5, pp. 794–796, May 1995.
- [52] A. Aronne *et al.*, “The origin of nanostructuring in potassium niobosilicate glasses by Raman and FTIR spectroscopy,” *J. Non. Cryst. Solids*, vol. 351, no. 46–48, pp. 3610–3618, Nov. 2005.
- [53] G. Blasse, G. J. Dirksen, M. P. Crosnier, and Y. Piffard, “The luminescence of $K_2(NbO)_2Si_4O_{12}$,” *J. Alloys Compd.*, vol. 189, no. 2, pp. 259–261, Dec. 1992.
- [54] F. Galasso and L. Katz, “Preparation and structure of $Ba_5Ta_4O_{15}$ and related compounds,” *Acta Crystallogr.*, vol. 14, no. 6, pp. 647–650, Jun. 1961.
- [55] R. Ratheesh, H. Sreemoolanadhan, and M. T. Sebastian, “Vibrational Analysis of $Ba_{5-x}Sr_xNb_4O_{15}$ Microwave Dielectric Ceramic Resonators,” *J. Solid State Chem.*, vol. 131, no. 1, pp. 2–8, Jun. 1997.
- [56] U. Balachandran and N. G. Eror, “Raman spectrum of the high temperature form of Nb_2O_5 ,” *J. Mater. Sci. Lett.*, vol. 1, no. 9, pp. 374–376, Sep. 1982.
- [57] A. E. L. Jazouli, C. Parent, G. L. E. Flem, and P. Hagemuller, “ $Na_4Nb (PO_4)_3$, a Material with a Reversible Crystal-Glass Transformation: Structural and Optical Comparison,” vol. 384, pp. 377–384, 1988.
- [58] A. F. Corsmit, H. E. Hoefdraad, and G. Blasse, “Vibrational spectra of ordered perovskites,” *J. Inorg. Nucl. Chem.*, vol. 34, no. 11, pp. 3401–3404, Nov. 1972.
- [59] G. Blasse and A. F. Corsmit, “Electronic and vibrational spectra of ordered perovskites,” *J. Solid State Chem.*, vol. 6, no. 4, pp. 513–518, Apr. 1973.
- [60] L. Guerbous and A. Boukerika, “Nanomaterial Host Bands Effect on the Photoluminescence Properties of Ce-Doped YAG Nanophosphor Synthesized by Sol-Gel Method,” *J. Nanomater.*, vol. 2015, pp. 1–10, 2015.
- [61] Z. Xinguo and G. Menglian, “Photoluminescence and energy transfer of Ce^{3+} , Tb^{3+} , Eu^{3+} doped $KBaY(BO_3)_2$ as NUV-excited color-tunable phosphors,” *Ind. Eng. Chem. Res.*, vol. 54, pp. 1–25, 2015.
- [62] C. C. Yu *et al.*, “Enhanced photoluminescence of $Ba_2GdNbO_6: Eu^{3+}/Dy^{3+}$ phosphors by Li^+ doping,” *J. Solid State Chem.*, vol. 180, no. 11, pp. 3058–3065, Nov. 2007.
- [63] G. Gasparotto, S. A. M. Lima, M. R. Davolos, J. A. Varela, E. Longo, and M. A. Zaghete, “Luminescence properties of Eu^{3+} - and Mg^{2+} -doped $LiTaO_3$ obtained

- via the polymeric precursor method,” *J. Lumin.*, vol. 128, no. 10, pp. 1606–1610, Oct. 2008.
- [64] V. Sivakumar and U. V. Varadaraju, “Synthesis, phase transition and photoluminescence studies on Eu^{3+} -substituted double perovskites—A novel orange-red phosphor for solid-state lighting,” *J. Solid State Chem.*, vol. 181, no. 12, pp. 3344–3351, Dec. 2008.
- [65] Y. Wu, F. Meng, Q. Li, M. Koschan, and C. L. Melcher, “Role of Ce^{4+} in the Scintillation Mechanism of Codoped $\text{Gd}_3\text{Ga}_3\text{Al}_2\text{O}_{12}:\text{Ce}$,” *Phys. Rev. Appl.*, vol. 2, no. 4, p. 044009, Oct. 2014.
- [66] J.-H. Maeng and S.-C. Choi, “The Effect of Cerium Reduction on Light Emission in Cerium-containing $20\text{Y}_2\text{O}_3\text{-}25\text{Al}_2\text{O}_3\text{-}55\text{SiO}_2$ Glass,” *J. Opt. Soc. Korea*, vol. 16, no. 4, pp. 414–417, Dec. 2012.
- [67] L. Guerbous and O. Krachni, “The 4f-5d luminescence transitions in cerium-doped LuF_3 ,” *J. Mod. Opt.*, vol. 53, no. 14, pp. 2043–2053, Sep. 2006.
- [68] P. Dorenbos, “5d -level energies of Ce^{3+} and the crystalline environment. I. Fluoride compounds,” *Phys. Rev. B*, vol. 62, no. 23, pp. 15640–15649, Dec. 2000.
- [69] N. P. Patel, M. Srinivas, D. Modi, V. Vishwnath, and K. V. R. Murthy, “Luminescence study and dosimetry approach of Ce on an $\alpha\text{-Sr}_2\text{P}_2\text{O}_7$ phosphor synthesized by a high-temperature combustion method,” *Luminescence*, vol. 30, no. 4, pp. 472–478, Jun. 2015.
- [70] K. Li, S. Liang, M. Shang, H. Lian, and J. Lin, “Photoluminescence and Energy Transfer Properties with Y+ SiO_4 Substituting Ba+ PO_4 in $\text{Ba}_3\text{Y}(\text{PO}_4)_3:\text{Ce}^{3+}/\text{Tb}^{3+}$, $\text{Tb}^{3+}/\text{Eu}^{3+}$ Phosphors for w-LEDs,” *Inorg. Chem.*, vol. 55, no. 15, pp. 7593–7604, Aug. 2016.
- [71] K. Binnemans, “Lanthanide-Based Luminescent Hybrid Materials,” *Chem. Rev.*, vol. 109, no. 9, pp. 4283–4374, Sep. 2009.
- [72] N. Tiwari, V. Dubey, J. Dewangan, and N. Jain, “Near UV-Blue Emission From Cerium Doped Zirconium Dioxide Phosphor for Display and Sensing Applications,” *J. Disp. Technol.*, vol. 12, no. 9, pp. 933–937, Sep. 2016.